Phase Equilibria, Thermodynamics and Solidified Microstructure in the Copper–Zirconium–Yttrium System

Fengting Jing [1], Yuling Liu [1,*], Yong Du [1,*], Chenying Shi [1], Biao Hu [2] and Xiancong He [3]

[1] State Key Laboratory of Powder Metallurgy, Central South University, Changsha 410083, China
[2] School of Materials Science and Engineering, Anhui University of Science and Technology, Huainan 232001, China
[3] School of Material Science and Engineering, Nanjing Institute of Technology, Nanjing 211167, China
* Correspondence: liu.yuling@csu.edu.cn (Y.L.); yong-du@csu.edu.cn (Y.D.); Tel.: +86-731-8887-7300 (Y.D.)

Abstract: A copper alloy with the addition of zirconium and yttrium is an attractive high strength and high conductivity (HSHC) copper alloy. The study of the solidified microstructure, thermodynamics and phase equilibria in the ternary Cu–Zr–Y system is expected to provide new insight into designing an HSHC copper alloy. In this work, the solidified and equilibrium microstructure and phase transition temperatures in the Cu–Zr–Y ternary system were studied by X-ray diffraction (XRD), electron probe microanalysis (EPMA) and differential scanning calorimeter (DSC). The isothermal section at 973 K was experimentally constructed. No ternary compound was found, while the Cu_6Y, Cu_4Y, Cu_7Y_2, Cu_5Zr, $Cu_{51}Zr_{14}$ and $CuZr$ phases substantially extended into the ternary system. According to the experimental phase diagram data from the present work and the literature, the Cu–Zr–Y ternary system was assessed using the CALPHAD (CALculation of PHAse diagrams) method. The isothermal sections, vertical section and liquidus projection calculated by the present thermodynamic description agree well with the experimental results. This study not only establishes a thermodynamic description of the Cu–Zr–Y system, but also contributes to the design of a copper alloy with the required microstructure.

Keywords: Cu–Zr–Y system; phase diagram; liquidus projection; CALPHAD; solidified microstructures

1. Introduction

Copper alloy has excellent electrical and thermal conductivity, good ductility and moderate strength. It is widely used in new energy, electrical and electronics, rail transit and so on [1–3]. With the continuous iterative development of products, the requirements for the properties of copper alloy are gradually increasing [4–8]. The high strength and high conductivity (HSHC) copper alloy is drawing growing interest. The influence of zirconium (Zr) on the properties of copper alloy has been systematically studied by many researchers [9–11]. Peng et al. [9] studied phase transition for the Cu-0.12 wt.% Zr alloy in the course of aging at 723 K and concluded that the Cu_5Zr precipitation contributes to the strength. Du et al. [10] investigated the Zr-containing precipitate evolution of the copper–chromium–zirconium alloy and noted that the yield strength was mainly influenced by the Cu_5Zr phase, Cr-rich precipitation and Zr-rich atomic clusters. To further improve the performance of copper alloy, more and more studies [12–16] have been conducted on the microstructure and properties influenced by the rare earth elements added to copper alloy. The properties for the copper–zirconium–yttrium alloy after cold-rolling and aging were studied systematically by Gao et al. [12] using selected area electron diffraction (SAED) and transmission electron microscopy (TEM), and they concluded that second-phase precipitation can be promoted by adding yttrium (Y). Wang et al. [15] noted that the addition of Y into a Cu–Cr alloy will inhibit the growth of Cr precipitation and decrease the dislocation density, thus increasing the ultimate tensile strength and hardness after cold-rolling and aging. As depicted above, the addition of Zr and Y can promote strength

during aging in copper alloy, and Cu–Zr–Y alloy is a key system for potential HSHC copper alloy. The aging process is driven by thermodynamics and knowledge of phase equilibrium and thermodynamics is essential to design compositions and optimize the aging process [17]. Therefore, obtaining an accurate thermodynamic description for the Cu–Zr–Y ternary system is expected to provide new insight into designing an HSHC copper alloy.

Thus far, only two studies on the phase equilibria of the Cu–Zr–Y system have been reported. He et al. [18] first determined the partial isothermal section at 978 K by an electron probe microanalysis (EPMA) technique applied to diffusion couples and extrapolated the ternary isothermal section according to the thermodynamic parameters of three binary systems. No ternary compound was found, and the solubilities of Y in the Cu–Zr system and those of Zr in the Cu–Y system were not considered. The crack in the diffusion-triple affected the results and eight three-phase regions were estimated in the Cu–Zr–Y system by alloy-sampling and diffusion-triple. He et al. [18] noted that measuring three-phase equilibrium was difficult due to electron scattering effects and the presence of a lot of small phase regions around the tri-junction points. Myronenko et al. [19] studied the isothermal section of the Cu–Zr–Y system at 870 K by the alloy annealed at 870 k for 720 h with X-ray diffraction (XRD) and microstructural analysis. The solubility of Y in the $Cu_{51}Zr_{14}$ phase was surprisingly high compared to $Cu_{51}Zr_{2.3}Y_{11.7}$, but no detailed experimental data were provided. The solubilities of Y in the Cu–Zr system and those of Zr in the Cu–Y system are still not clearly characterized.

Further experimental studies for the Cu–Zr–Y system are therefore warranted to provide basic information for the thermodynamic description. The purposes of this work are (1) to experimentally investigate the solidification and equilibrium microstructure and phase transition temperatures in the Cu–Zr–Y system; (2) to evaluate experimental data from the present work and literature to optimize thermodynamic parameters; and (3) to calculate the phase diagram and perform the Scheil solidification simulations.

2. Experimental Procedure

The purities of the elements used were Cu-99.99 wt.%, Zr-99.95 wt.% and Y-99.99 wt.%. The alloys were prepared in an arc furnace (WKDHL-1, Opto-electronics Co. Ltd., Beijing, China) with a water-cooled copper crucible in a highly pure argon environment. The alloys were flipped and remelted at least four times to ensure uniformity. The weight of each sample was usually between 4–6 g. The weight loss of every alloy was lower than 2.5%. The real overall composition of the alloys was determined through inductively coupled plasma-optical emission spectrometry (ICP-OES, Thermo Fisher Scientific Inc., Waltham, MA, USA). Each alloy was cut into two parts using wire electrical discharge machining (EDM). One part was analyzed as an as-cast alloy. The other part was encapsulated in a vacuum quartz pipe. A total of 12 samples were melted and numbered sequentially as A1–A12, and their compositions are listed in Table 1. Alloys A1–A8 were annealed at 973 K for 40 days, then water quenched. Alloys A9–A12 were annealed at 1073 K for 40 h, and then annealed at 973 K for 30 days and finally water quenched. XRD (Bruker-AXS D8) and EPMA with wavelength dispersive X-ray spectroscopy (WDX) (JXA-8230, JEOL, Japan) were then used to determine the microstructure and components of these alloys. Afterwards, differential scanning calorimeter (DSC, Netzsch, Germany) measurements of the phase change temperatures of the annealed alloys were performed. The DSC device was performed in an Al_2O_3 crucible under a continuous flow of argon (99.998 wt.% purity) with a heating rate of 5 K/min from 303 K to 1323 K. The temperatures for the invariant reactions and liquidus were defined by the initial and peak temperatures, respectively.

Table 1. Summary of the experimental data for the Cu–Zr–Y system.

Alloy No.	Alloy Composition (at.%)	Primary Phase	Primary Phase Composition (at.%)			Solidification Paths	Phase Equilibria	Equilibrium Phase Composition (at.%)		
			Cu	Y	Zr			Cu	Y	Zr
A1	Cu90Zr8Y2	Cu_5Zr	83.05	1.05	15.9	$L \rightarrow Cu_5Zr$	(Cu)	99.95	0	0.05
						$L \rightarrow (Cu) + Cu_5Zr$	Cu_5Zr	83.22	2.03	14.75
						$L \rightarrow (Cu) + Cu_5Zr + Cu_6Y$	Cu_6Y	84.69	8.7	6.61
A2	Cu88Zr5Y7	Cu_5Zr	82.84	7.08	10.08	$L \rightarrow Cu_{51}Zr_{14}$	(Cu)	99.62	0.15	0.23
						$L + Cu_{51}Zr_{14} \rightarrow Cu_5Zr$	Cu_5Zr	82.20	2.57	15.23
						$L \rightarrow (Cu) + Cu_5Zr$	Cu_6Y	84.26	9.84	5.9
A3	Cu69Zr10Y21	Cu_7Y_2	77.18	17.00	5.82	$L \rightarrow Cu_7Y_2$	$Cu_{10}Zr_7$	59.74	1.53	38.73
						$L \rightarrow Cu_7Y + Cu_2Y$	Cu_2Y	67.59	31.79	0.62
						$L + Cu_7Y_2 \rightarrow Cu_{10}Zr_7 + Cu_2Y$	Cu_7Y_2	78.79	13.38	7.83
A4	Cu33Zr7Y60	(αY)	4.78	94.28	0.94	$L \rightarrow (\alpha Y)$	(αY)	2.06	97.26	0.68
						$L \rightarrow (\alpha Y) + (\alpha Zr)$	(αZr)	2.81	1.51	95.68
						$L \rightarrow (\alpha Y) + (\alpha Zr) + CuY$	CuY	49.64	49.76	0.60
A5	Cu87Zr2Y11	Cu_6Y	84.25	11.12	4.63	$L \rightarrow Cu_6Y$	(Cu)	98.80	1.19	0.01
						$L \rightarrow Cu_6Y + (Cu)$	Cu_6Y	85.34	11.56	3.1
A6	Cu86Zr13Y1	$Cu_{51}Zr_{14}$	79.46	0.13	20.41	$L \rightarrow Cu_{51}Zr_{14}$	(Cu)	98.98	0.16	0.86
						$L + Cu_{51}Zr_{14} \rightarrow Cu_5Zr$	Cu_5Zr	83.07	1.04	15.89
						$L \rightarrow (Cu) + Cu_5Zr$				
A7	Cu79Zr13Y8	$Cu_{51}Zr_{14}$	79.17	3.72	17.11	$L \rightarrow Cu_{51}Zr_{14}$	$Cu_{51}Zr_{14}$	78.87	3.99	17.14
						$L \rightarrow Cu_4Y$	Cu_4Y	79.88	13.85	6.27
A8	Cu48Zr41Y11	$CuZr_2$	34.52	0.04	65.44	$L \rightarrow CuZr_2$	$CuZr_2$	34.55	0.1	65.35
						$L \rightarrow CuZr + CuZr_2$	CuZr	50.54	3.38	46.08
						$L + CuZr \rightarrow Cu_2Y + CuZr_2$	Cu_2Y	67.38	30.50	2.12
A9	Cu53Zr12Y35	CuY	50.14	46.08	3.78	$L \rightarrow CuY$	CuY	50.76	47.43	1.81
						$L \rightarrow CuY + Cu_2Y$	Cu_2Y	67.05	32.95	0
						$L \rightarrow CuY + Cu_2Y + CuZr_2$	$CuZr_2$	34.78	0	65.22
A10	Cu22Zr71Y7	(αZr)	4.34	0	95.66	$L \rightarrow (\alpha Zr)$	(αZr)	2.28	0	97.72
						$L \rightarrow (\alpha Zr) + CuZr_2$	$CuZr_2$	34.06	0	65.94
						$L \rightarrow (\alpha Zr) + CuZr_2 + CuY$	CuY	49.09	48.78	2.13
A11	Cu78Zr18Y4	$Cu_{51}Zr_{14}$	79.10	6.16	14.74	$L \rightarrow Cu_{51}Zr_{14}$	$Cu_{51}Zr_{14}$	78.80	4.42	16.78
						$L \rightarrow Cu_{10}Zr_7 + Cu_{51}Zr_{14}$	$Cu_{10}Zr_7$	59.82	0.31	39.87
A12	Cu66Zr32Y2	$Cu_{51}Zr_{14}$	73.39	1.87	24.73	$L \rightarrow Cu_{51}Zr_{14}$	$Cu_{51}Zr_{14}$	78.23	4.45	17.32
						$L \rightarrow Cu_{10}Zr_7 + Cu_{51}Zr_{14}$	$Cu_{10}Zr_7$	59.66	0.01	40.33

3. Thermodynamic Models

The phase diagram of the Cu–Y system was minutely adjusted in the present work based on the work of Fries et al. [20]. The phase diagrams of the Cu–Zr system by Liu et al. [21] and the Zr–Y system by Bu et al. [22] are accepted in this work due to the consistency of the thermodynamic databases of copper alloy [23–26]. The crystallographic data for stable phases in the Cu–Zr–Y system are shown in Table S1 [20,27–35] in the supporting information. The calculated binary sub-systems phase diagrams are shown in Figures 1–3.
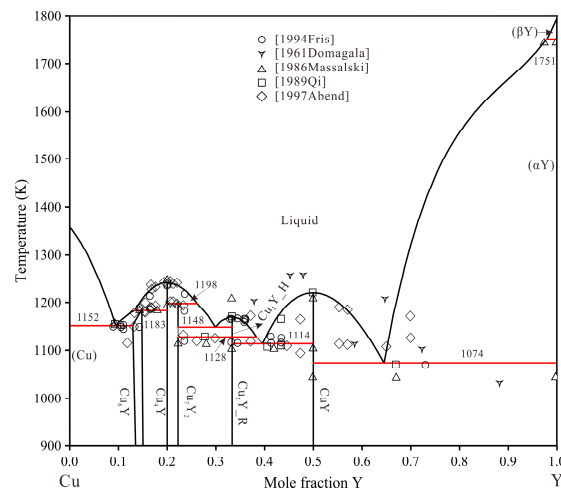
Figure 1. Calculated Cu–Y phase diagram using the parameter from Fries et al. [20] and this work.
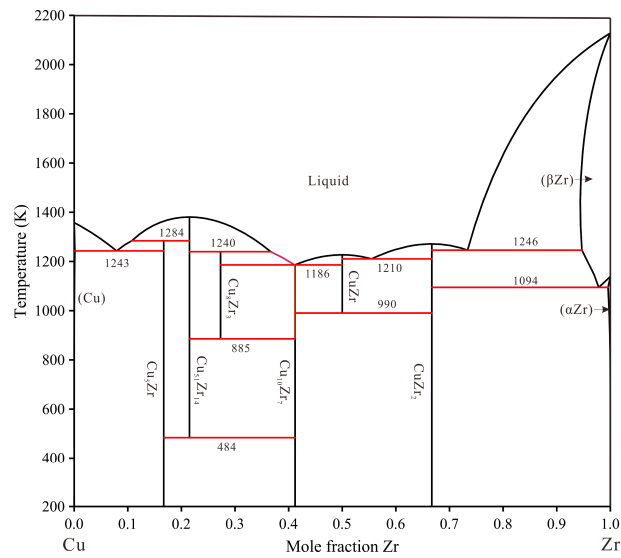
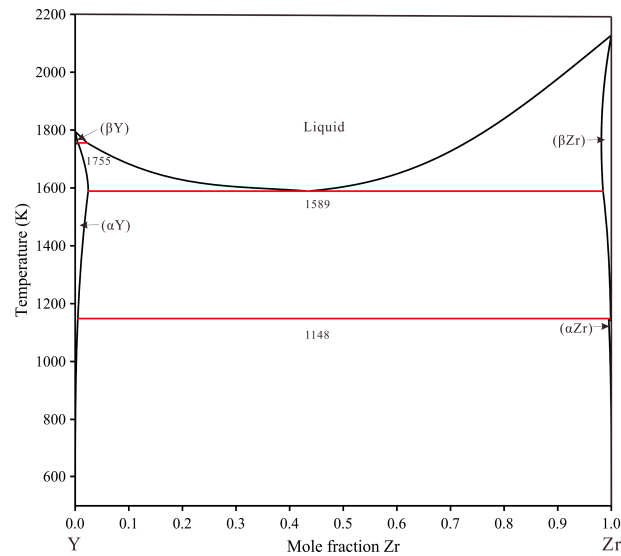**Figure 2.** Calculated Cu–Zr phase diagram using the parameter from Liu et al. [21].

Figure 3. Calculated Y–Zr phase diagram using the parameter from Bu et al. [22].

3.1. Pure Elements

The Gibbs energy function for the pure element *i* (*i*= Cu, Zr and Y) is taken from the Scientific Group Thermodata Europe (SGTE) by Dinsdale [36] and described in the form of:

$$G_i(T) - H_i^{SER} = a + bT + cT \cdot \ln T + dT^2 + eT^{-1} + fT^3 + iT^7 + jT^{-9} \tag{1}$$

where H_i^{SER} means the mole enthalpy of element *i* relative to the stable element reference (SER) at 298.15 K and 1 bar, and *T* is the absolute temperature in Kelvin.

3.2. The Solution Phases

In the Cu–Y and Cu–Zr–Y systems, (Cu) is the fcc phase, (αZr) and (αY) are the hcp phases (βZr) and (βY) are the bcc phases. The liquid, fcc, hcp and bcc phases serve as a substitutional solution model. The molar Gibbs free energy of the solution phase is described as follows:

$$^0G^{\varphi} - H^{SER} = \sum_i x_i \,^0G_i^{\varphi} + RT\sum_i x_i \ln(x_i) + {}^{ex}G_m^{\varphi} \tag{2}$$

where x_i is the mole fraction of element i (i= Cu, Zr and Y); $^0G_i^\varphi$ denotes the molar Gibbs energy of component i in the state phase φ; and R represents the gas constant. $^{ex}G_m^\varphi$ represents the excess Gibbs energy, which is described by the Redlich–Kister (R–K) [37] polynomial. In the Cu–Zr–Y system, $^{ex}G_m^\varphi$ is represented as follows.

$$
\begin{aligned}
^{ex}G_m^\varphi = \quad & x_{Cu}x_Y\sum_{m=0,1...} {}^mL_{Cu,Y}^\varphi(x_{Cu}-x_Y)^m + x_{Cu}x_{Zr}\sum_{m=0,1...} {}^mL_{Cu,Y}^\varphi(x_{Cu}-x_{Zr})^m \\
& + x_Yx_{Zr}\sum_{m=0,1...} {}^mL_{Y,Zr}^\varphi(x_Y-x_{Zr})^m + x_{Cu}x_Yx_{Zr}L_{Cu,Y,Zr}^\varphi
\end{aligned}
\tag{3}
$$

where $^mL_{i,j}^\varphi$ is the mth binary interaction parameter, which can be shown by:

$$
{}^mL_{i,j}^\varphi = a_m + b_mT
\tag{4}
$$

where $L_{Cu,Y,Zr}^\varphi$ is ternary interaction parameter, which can be shown by:

$$
L_{Cu,Y,Zr}^\varphi = x_{Cu}{}^0L_{Cu,Y,Zr}^\varphi + x_Y{}^1L_{Cu,Y,Zr}^\varphi + x_{Zr}{}^2L_{Cu,Y,Zr}^\varphi
\tag{5}
$$

The interaction parameters were optimized in this work based on the available experimental data.

3.3. Intermetallic Compounds

There are 11 intermetallic compounds in the system. The Cu_2Y, CuY, Cu_8Zr_3, $Cu_{10}Zr_7$ and $CuZr_2$ phases with ignorable homogeneity are considered as stoichiometric compounds according to the literature and current experimental data, whose Gibbs energy description is given as follows:

$$
G_{A_mB_n} = m^0G_A^{HSER} + n^0G_B^{HSER} + a + bT
\tag{6}
$$

where m and n stand for the ratios of stoichiometry and $^0G_A^{HSER}$ and $^0G_B^{HSER}$ represent the molar Gibbs energy referring to the SER states of A and B, respectively.

The Cu_4Y, Cu_6Y, Cu_7Y_2, Cu_5Zr, $Cu_{51}Zr_{14}$ and $CuZr$ phases with solubilities of a third element were described by a two-sublattice model. Take a phase φ modeled as $(A,\ B)_p(A,\ C)_q$ for example. The molar Gibbs energy formula is given as Equation (7):

$$
\begin{aligned}
G_m^\varphi = & \; y_A'y_A''G_{A:A}^\varphi + y_A'y_C''G_{A:C}^\varphi + y_B'y_A''G_{B:A}^\varphi + y_B'y_C''G_{B:C}^\varphi \\
& + RT[p(y_A'\ln y_A' + y_B'\ln y_B') + q(y_A''\ln y_A'' + y_C''\ln y_C'') \\
& + y_A'y_B'\left(y_A''\sum_i {}^iL_{A,B:A}^\varphi(y_A'-y_B')^i + y_C''\sum_i {}^iL_{A,B:C}^\varphi(y_A'-y_B')^i\right) \\
& + y_A''y_C''\left(y_A'\sum_i {}^iL_{A:A,C}^\varphi(y_A''-y_C'')^i + y_B'\sum_i {}^iL_{B:A,C}^\varphi(y_A''-y_C'')^i\right)
\end{aligned}
\tag{7}
$$

where y_A' and y_A'' are the fraction of the constituent A in the first and second sublattice, respectively. ^iL represents the ith optimized interaction parameter in this work.

4. Results and Discussion

4.1. Microstructure and Phase Transition Temperatures Analysis

In this work, twelve alloys were prepared to determine the primary phase and phase equilibria of the Cu–Zr–Y system at 973 K. Table 1 summarizes the results measured by EPMA and XRD, including the primary phase and solidification paths of the as-cast alloy, as well as the equilibria phases of the annealed alloy. In this work, eight primary phases, i.e., (αY), (αZr), $CuZr_2$, $Cu_{51}Zr_{14}$, Cu_5Zr, CuY, Cu_7Y_2 and Cu_6Y, were found. The representative alloys are discussed in detail below. Table 2 lists the temperatures of the invariant reactions and liquidus measured by DSC.

Table 2. Comparison of the DSC results with the calculated results in the Cu–Zr–Y system.

Alloy No.	Alloy Composition (at.%)	Phase Transition Temperatures (K)			
		Liquidus		Invariant	
		Exp.	Calc.	Exp.	Calc.
A1	Cu90Zr8Y2	1253	1252		
		1223	1217		
A2	Cu88Zr5Y7	1225	1197	1149	1149
A3	Cu69Zr10Y21	1143	1141		
A4	Cu33Zr7Y60	1093	1090		
A5	Cu87Zr2Y11	1180	1179		
		1153	1151		
A6	Cu86Zr13Y1	1223	1217		
A7	Cu79Zr13Y8	1295	1299		

4.1.1. Microstructure of Solidification

Figure 4a,d presents the back-scattered electron (BSE) micrograph and XRD pattern of the as-cast alloy A1 $Cu_{90}Zr_8Y_2$ (at.%). The primary phase in the images is shown in bold. The analysis shows that the gray phase of Cu_5Zr is the primary phase, and there are a lot of eutectic structures around it. During the arc-melting process, the side close to the copper crucible cools faster and the solidified microstructure is coarser, while the microstructure further away from crucible is finer. As shown in Figure 4a, the microstructure on the right is coarser than that on the left side. The coarser and finer microstructures in one alloy were also found in our previous Ag–Cr–Zr alloy [24]. Combined with the XRD results, the eutectic structure should be composed of $(Cu) + Cu_5Zr + Cu_6Y$. It can be postulated that the Cu_5Zr phase solidifies first during the solidification process. Then the liquidus transformation component point soon contacts $L \rightarrow (Cu) + Cu_5Zr$ eutectic reaction. Finally, the eutectic equilibrium reaction of $L \rightarrow (Cu) + Cu_5Zr + Cu_6Y$ occurs quickly, therefore a large number of eutectic structures are formed. Figure 5 shows a representative DSC curve for the A1 alloy with a heating rate of 5K/min. There are two visible peaks on this curve. Combined with the previous solidification analysis, the onset temperature of 1123 K of the first peak corresponds to the reaction of $L \rightarrow (Cu) + Cu_5Zr$. The peak temperature of 1153 K of the second peak corresponds to the liquidus temperature of the alloy.
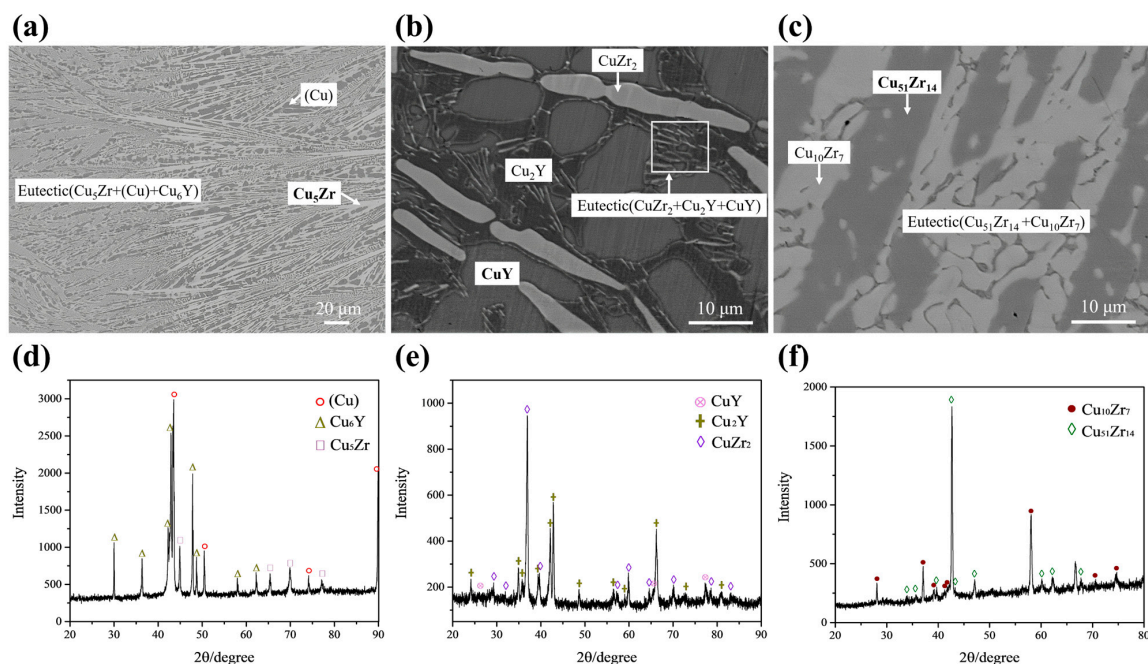

Figure 4. BSE micrographs and XRD patterns of as-cast alloys: (**a**,**d**) A1 $Cu_{90}Zr_8Y_2$ (at.%); (**b**,**e**) A9 $Cu_{53}Zr_{12}Y_{35}$ (at.%); (**c**,**f**) A12 $Cu_{66}Zr_{32}Y_2$ (at.%).

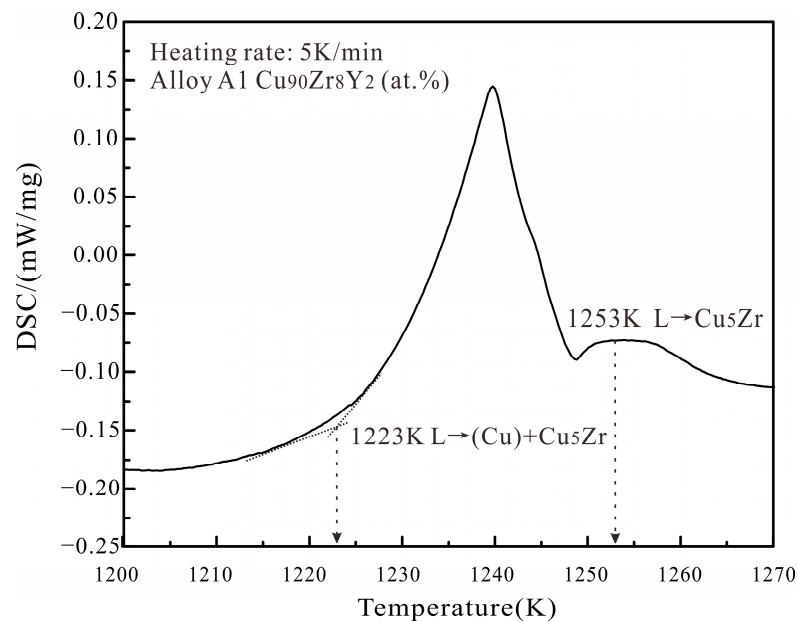**Figure 5.** The DSC curves with a heating rate of 5 K/min for annealed alloy A1 $Cu_{90}Zr_8Y_2$ (at.%) of the Cu–Zr–Y system.

Figure 4b,e presents the BSE micrograph and XRD pattern of the as-cast alloy A9 $Cu_{53}Zr_{12}Y_{35}$ (at.%). There are bright phase $CuZr_2$, gray phase CuY, black phase Cu_2Y and a eutectic structure of $CuZr_2 + CuY + Cu_2Y$ noted in the white rectangle. The solidification paths of A9 are $L \rightarrow CuZr_2$, $L \rightarrow CuZr_2 + CuZr$ and $L \rightarrow CuZr_2 + Cu_2Y + CuZr$.

Figure 4c,f presents the BSE micrograph and XRD pattern of the as-cast alloy A12 $Cu_{66}Zr_{32}Y_2$ (at.%). There are gray phase $Cu_{10}Zr_7$, dark gray phase $Cu_{51}Zr_{14}$ and a eutectic structure of $Cu_{10}Zr_7 + Cu_{51}Zr_{14}$ in the alloy. Combined with the as-cast microstructure and XRD results, the primary phase of A12 is $Cu_{51}Zr_{14}$, although the composition of $Cu_{51}Zr_{14}$ in the as-cast alloy deviates slightly from the equilibrium phase composition shown in Table 1. The solidification paths of A12 are $L \rightarrow Cu_{51}Zr_{14}$ and $L \rightarrow Cu_{10}Zr_7 + Cu_{51}Zr_{14}$.

4.1.2. Microstructure of Annealed Alloys

The experimental results of 12 alloys annealed at 973 K are summarized in Table 1. No ternary compound exists. Four two-phase regions, i.e., $(Cu) + Cu_6Y$, $(Cu) + Cu_5Zr$, $Cu_{51}Zr_{14} + Cu_4Y$, $Cu_{51}Zr_{14} + Cu_{10}Zr_7$, and six three-phase regions, i.e., $(Cu) + Cu_6Y + Cu_5Zr$, $Cu_{10}Zr_7 + Cu_2Y + Cu_7Y_2$, $(\alpha Y) + (\alpha Zr) + CuY$, $Cu_2Y + CuZr_2 + CuZr$, $Cu_2Y + CuZr_2 + CuY$, $(\alpha Zr) + CuZr_2 + CuY$, are determined experimentally. The relationships are discussed as follows.

Figure 6a,d shows the BSE micrograph and XRD pattern for alloy A1 $Cu_{90}Zr_8Y_2$ (at.%), respectively. The annealed microstructure of alloy A1 is similar to that of the cast state shown in Figure 4a. The XRD result indicates the presence of the Cu_6Y phase and the BSE micrograph illustrates the presence of the Cu_6Y phase in the eutectic microstructure. Therefore, in conjunction with the analysis above, alloy A1 consists of white Cu_5Zr, gray Cu_6Y and black (Cu). The solubility of Y in Cu_5Zr is 2.03 at.%. The solubility of Zr in Cu_6Y is 6.61 at.%. Figure 6b,e shows the BSE micrograph and XRD pattern for alloy A3 $Cu_{69}Zr_{10}Y_{21}$ (at.%), respectively. The annealing alloy A3 is composed of $Cu_{10}Zr_7$ (white), Cu_2Y (gray) and Cu_7Y_2 (dark). The concave–convex morphology of the Cu_7Y_2 phase and Cu_2Y phase is the same as the result of He et al. [18]. The solubility of Y in $Cu_{10}Zr_7$ is 1.53 at.%. The solubility of Zr in Cu_7Y_2 is 7.83 at.%. Figure 6c,f shows the BSE micrograph and XRD pattern for alloy A8 $Cu_{48}Zr_{41}Y_{11}$ (at.%), respectively. According to the results, alloy A8 is located in the three-phase region, i.e., bright $CuZr_2$, grey $CuZr$ and black Cu_2Y. The solubility of Y in $CuZr$ is 3.38 at.%.
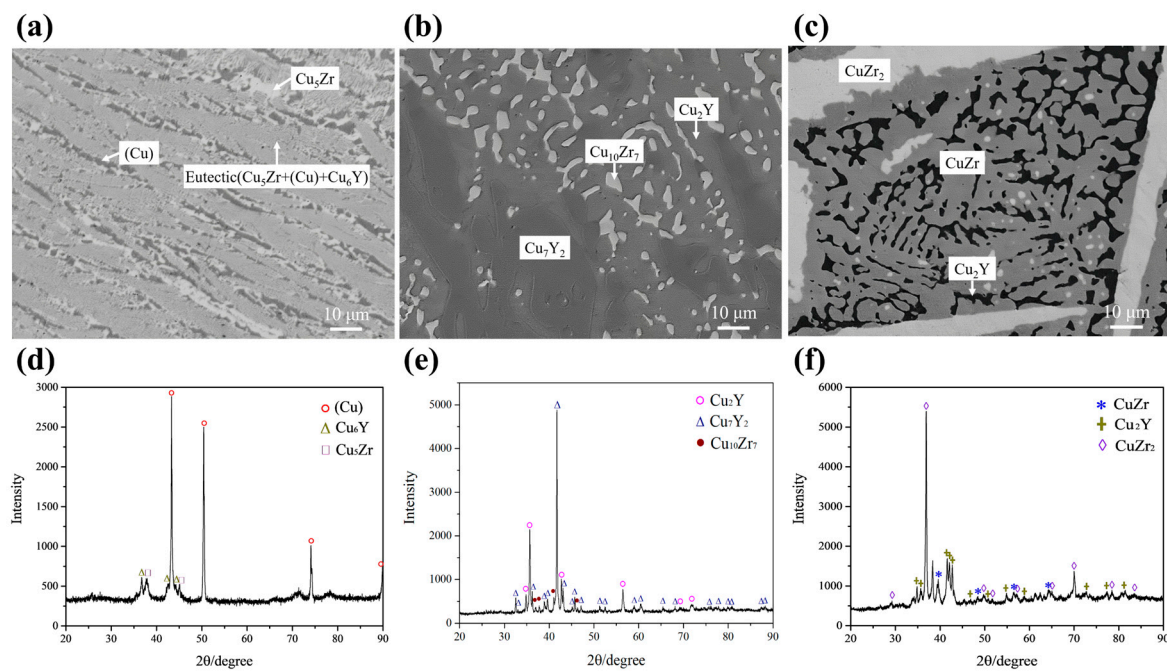
Figure 6. BSE micrographs and XRD patterns of annealed alloys: (**a**,**d**) A1 $Cu_{90}Zr_8Y_2$ (at.%); (**b**,**e**) A3 $Cu_{69}Zr_{10}Y_{21}$ (at.%); (**c**,**f**) A8 $Cu_{48}Zr_{41}Y_{11}$ (at.%).

Figure 7a,d shows the BSE micrograph and XRD pattern for alloy A7 $Cu_{79}Zr_{13}Y_8$ (at.%), respectively. The results show that alloy A7 consists of light gray $Cu_{51}Zr_{14}$ and dark gray Cu_4Y phases. The A7 alloy is located in the two-phase region of $Cu_{51}Zr_{14}$ and Cu_4Y. Figure 7b,e and Figure 7c,f show the BSE micrographs and XRD patterns for alloys A11 $Cu_{78}Zr_{18}Y_4$ (at.%) and A12 $Cu_{66}Zr_{32}Y_2$ (at.%), respectively. In the standard PDF cards for the $Cu_{51}Zr_{14}$ and $Cu_{10}Zr_7$ phases, there is no standard peak after 77.757° of 2θ, therefore the peak larger than 78° is not calibrated in the XRD pattern. According to the results, alloys A11 and A12 are both located in the grey $Cu_{10}Zr_7$ and dark gray $Cu_{51}Zr_{14}$ two-phase region, although their microstructures differ considerably. More $Cu_{51}Zr_{14}$ phases are present in alloy A11. The measured maximum solubility of Y in $Cu_{51}Zr_{14}$ is about 4.45 at.%. The solubilities of the 3rd element are determined in this work for the Cu–Zr–Y system. Noticeable solubilities were also measured in the Al–Zr–Y system by Liu et al. [38] and Bao et al. [39].

Figure 8a,d shows the BSE micrograph and XRD pattern for alloy A4 $Cu_{33}Zr_7Y_{60}$ (at.%), respectively. The results show that alloy A4 is in the three-phase region for white αZr, grey αY and dark CuY. The rare earth Y is chemically active [40]. The oxidation of Y can be observed during the metallographic polishing process, which does not affect the phase equilibrium after vacuum annealing at 973 K. Combined with the XRD result, the black Y-oxide is Y_2O_3. The solubility of Cu in the hcp phase is about 2 at.%. Figure 8b,e shows the BSE micrograph and XRD pattern for alloy A9 $Cu_{53}Zr_{12}Y_{35}$ (at.%), respectively. The diagrams show that alloy A9 is in the three-phase region for white $CuZr_2$, grey CuY and black Cu_2Y. Figure 8c,f shows the BSE micrograph and XRD pattern for alloy A10 $Cu_{22}Zr_{71}Y_7$ (at.%), respectively. The diagrams show that alloy A10 is in the three-phase region for white αZr, grey $CuZr_2$ and dark CuY.

Based on the present experiments, the isothermal section at 973 K is constructed in Figure 9. Three two-phase regions and four three-phase regions agree well with those of He et al. [18]. The red dashed line in the experimental phase diagram indicates the phase regions that were not directly measured by the experiment. The alloys designed in the three-phase region of $Cu_4Y + Cu_6Y + Cu_5Zr$ tend to shift into the three-phase region of (Cu) + Cu_6Y + Cu_5Zr due to the small range of the phase region and the easy volatilization of Y during melting. This part has not been experimentally determined.
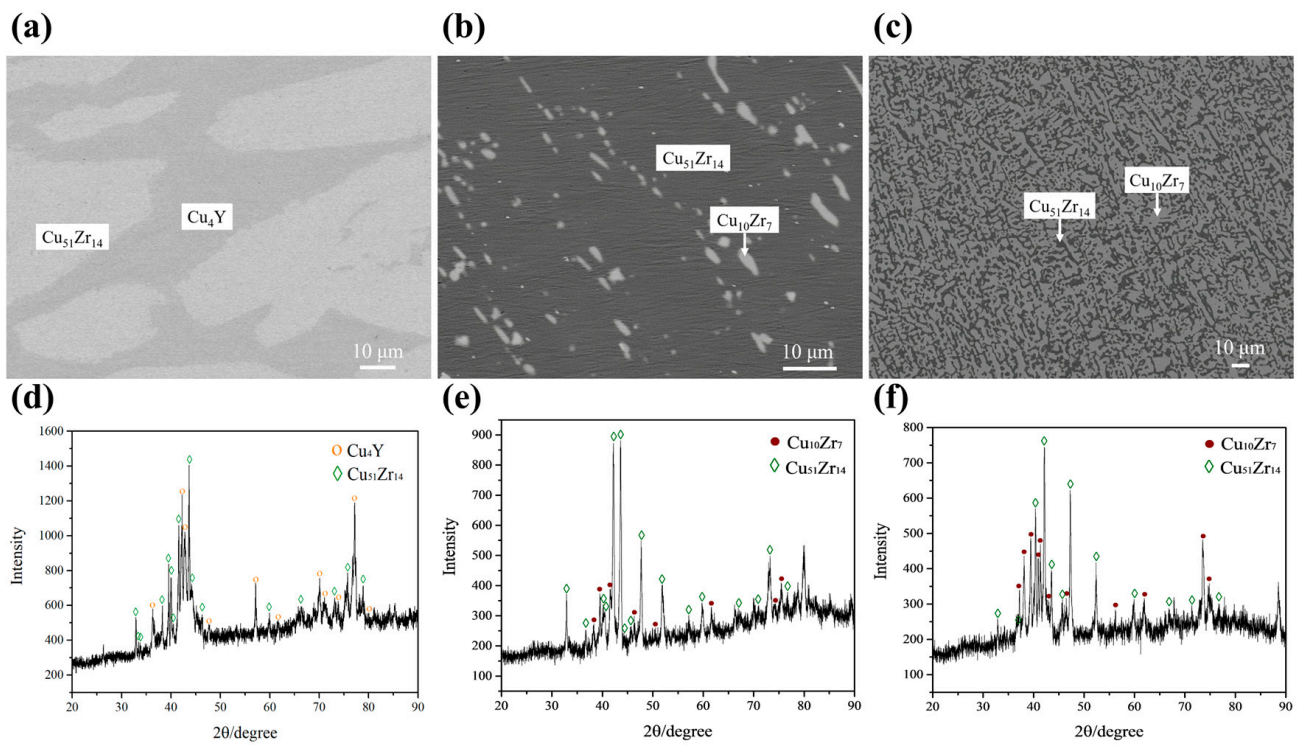
(a)

(b)

(c)

(d)

(e)

(f)

Figure 7. BSE micrographs and XRD patterns of annealed alloys: (**a**,**d**) A7 $Cu_{79}Zr_{13}Y_8$ (at.%); (**b**,**e**) A11 $Cu_{78}Zr_{18}Y_4$ (at.%); (**c**,**f**) A12 $Cu_{66}Zr_{32}Y_2$ (at.%).

(a)

(b)

(c)

(d)

(e)

(f)
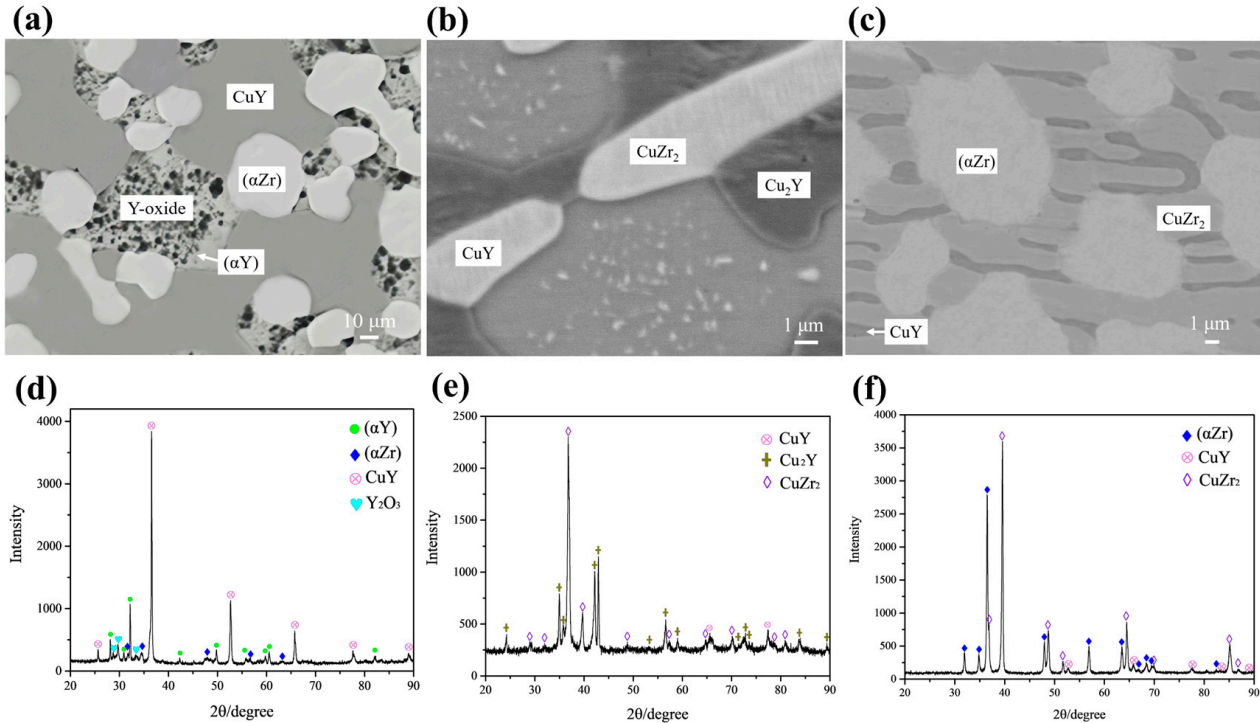
Figure 8. BSE micrographs and XRD patterns of annealed alloys: (**a**,**d**) A4 $Cu_{33}Zr_7Y_{60}$ (at.%); (**b**,**e**) A9 $Cu_{53}Zr_{12}Y_{35}$ (at.%); (**c**,**f**) A10 $Cu_{22}Zr_{71}Y_7$ (at.%).
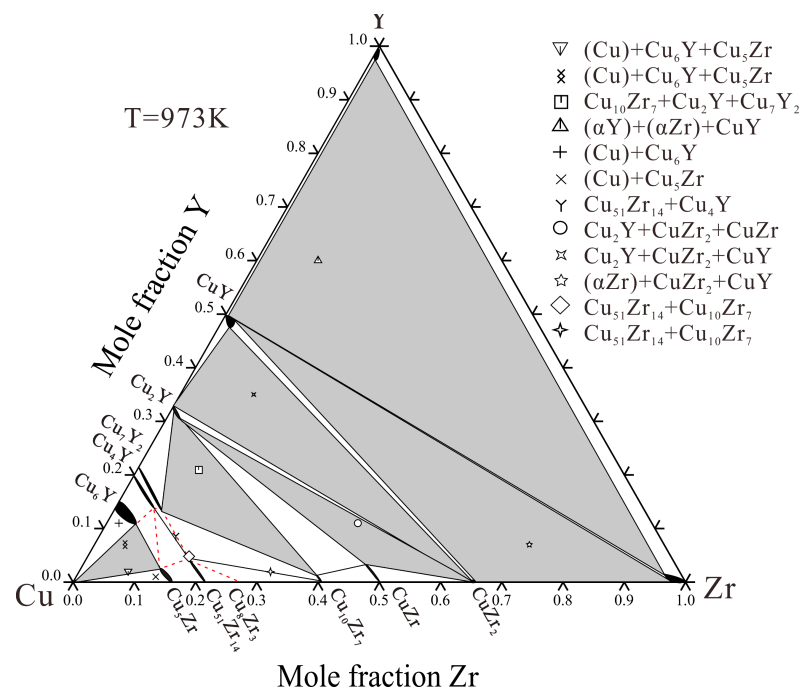
Figure 9. Experimental isothermal section of Cu–Zr–Y system with experimental data at 973 K.

4.2. Thermodynamic Assessment

The PARROT module in Thermo-Calc software [41] was used for optimization based on the least square method. The thermodynamic descriptions for the Cu–Y [20], Cu–Zr [21] and Zr–Y [22] systems in the literature were combined to form a basis for the Cu–Zr–Y system assessment. Before optimizing the ternary system, the thermodynamic parameters of Cu−Y were optimized in order to satisfy the phase relations of $(\alpha Y) + (\alpha Zr) + CuY$ and $(\alpha Zr) + CuZr_2 + CuY$ at 870K of the Cu–Zr–Y system. After optimization the temperature of the invariant reaction $(\alpha Zr) + CuY \rightarrow (\alpha Y) + CuZr_2$ was adjusted downward to 860 K. The presently calculated phase diagram of the Cu–Y system is consistent with the experimental data [20,42–44] and the calculated date [45], which is shown in Figure 1. For the Cu–Zr–Y system, the experimental data measured by alloy-sampling from the literature [18] are also used in the optimization.

Then the measured ternary solubilities of Cu_6Y, Cu_4Y, Cu_7Y_2, Cu_5Zr and $Cu_{51}Zr_{14}$ were considered. Optimization was carried out sequentially from the copper-rich end to the copper-poor end. Afterward, all the parameters were optimized simultaneously to achieve reasonable thermodynamic parameters. Finally, Table 3 provides the reasonable parameters of the Cu–Zr–Y system obtained in this work where the adjusted parameters are bolded. According to the current thermodynamic parameters, the calculated isothermal sections at 870 K, 973 K and 978 K are shown in Figure 10 compared with the reported experimental data [18,19] and the present measurement results. These calculations are in good agreement with experimental data. The calculated vertical section of the Cu–Zr–Y system at 10 at.% Zr, compared with the measured temperatures by DSC, are shown in Figure 11. It is noteworthy that only alloy A3 is located at the 10 at.% Zr vertical section. Alloy A2 is labeled in the vertical section by $L \rightarrow (Cu) + Cu_5Zr + Cu_6Y$ invariant reactions.

Figure 12 shows the calculated liquidus projection in comparison with the experimental primary phases. The present thermodynamic parameters are used for Scheil solidification simulation to guide the solidification behavior. Figure 13 shows the Scheil solidification simulation results of alloys A1 and A9. It can be seen that the primary phases of alloys A1 and A9 are Cu_5Zr and CuY, respectively. The ternary eutectic structure of $(Cu) + Cu_5Zr + Cu_6Y$ and $CuZr_2 + Cu_2Y + CuZr$ are formed. These Scheil solidification simulations are consistent with the experimental result discussed in Section 4.1.1.

Table 3. The thermodynamic parameters obtained in this work.

| Phases	Models	Thermodynamic Parameters
Liquid	$(Cu,Y,Zr)_1$	$^0G_{Cu,Y}^{Liquid} = -89300 + 21.5669 \cdot T$
		$^1L_{Cu,Y,Zr}^{Liquid} = 2000$
CuZr	$(Cu)_1(Zr,Y)_1$	$^0G_{Cu:Y}^{CuZr} = -11582 + {}^0G_{Cu}^{Fcc} + {}^0G_Y^{Hcp}$
$Cu_{51}Zr_{14}$	$(Cu)_{51}(Zr,Y)_{14}$	$^0G_{Cu:Y}^{Cu_{51}Zr_{14}} = -896480 + 51 \cdot {}^0G_{Cu}^{Fcc} + 14 \cdot {}^0G_Y^{Hcp}$
Cu_5Zr	$(Cu)_5(Zr,Y)_1$	$^0G_{Cu:Y}^{Cu_5Zr} = -64998 + 5 \cdot {}^0G_{Cu}^{Fcc} + {}^0G_Y^{Hcp}$
Cu_4Y	$(Cu)_4(Y,Zr)_1$	$^0G_{Cu:Y}^{Cu_4Y} = -89500 + 8.25205 \cdot T + 4 \cdot {}^0G_{Cu}^{Fcc} + {}^0G_Y^{Hcp}$
		$^0G_{Cu:Zr}^{Cu_6Y} = -40366 + 4 \cdot {}^0G_{Cu}^{Fcc} + {}^0G_{Zr}^{Hcp}$
Cu_6Y	$(Cu)_5(Cu2,Y,Zr)_1$	$^0G_{Cu:Y}^{Cu_6Y} = -90000 + 8.29539 \cdot T + 5 \cdot {}^0G_{Cu}^{Fcc} + {}^0G_{Zr}^{Hcp}$
		$^0G_{Cu:Zr}^{Cu_6Y} = -45447 + 5 \cdot {}^0G_{Cu}^{Fcc} + {}^0G_{Zr}^{Hcp}$
Cu_7Y_2	$(Cu)_7(Y,Zr)_2$	$^0G_{Cu:Y}^{Cu_7Y_2} = -168880 + 15.56757 \cdot T + 7 \cdot {}^0G_{Cu}^{Fcc} + 2 \cdot {}^0G_{Zr}^{Hcp}$
		$^0G_{Cu:Zr}^{Cu_7Y_2} = -55642 + 7 \cdot {}^0G_{Cu}^{Fcc} + 2 \cdot {}^0G_{Zr}^{Hcp}$
		$^0L_{Cu:Y,Zr}^{Cu_7Y_2} = -35442$
CuY	$(Cu)_1(Y)_1$	$^0G_{Cu:Y}^{CuY} = -44760 + 4.12 \cdot T + {}^0G_{Cu}^{Fcc} + {}^0G_Y^{Hcp}$
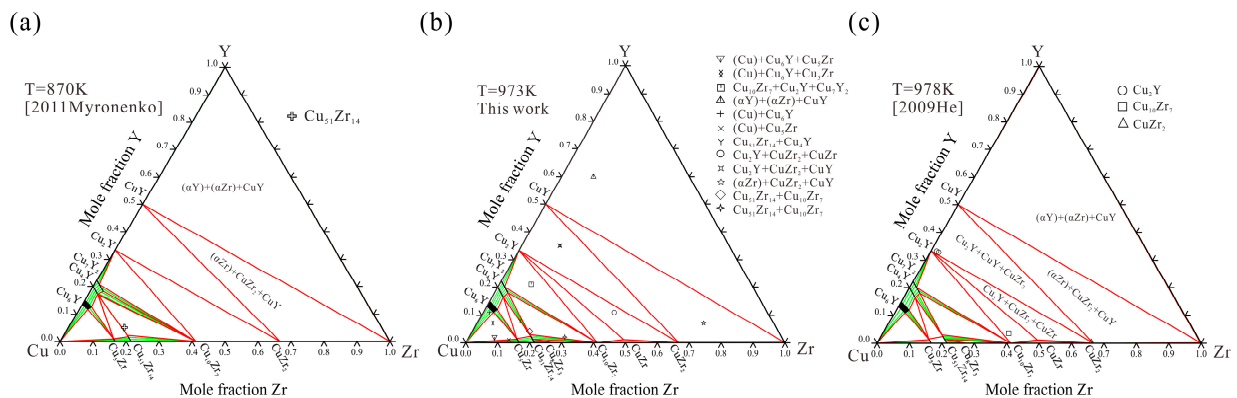
Figure 10. Calculated isothermal sections of Cu–Zr–Y system at (**a**) 870 K with experimental data [19], (**b**) 973 K with experimental data from this work and (**c**) 978 K with experimental data [18].
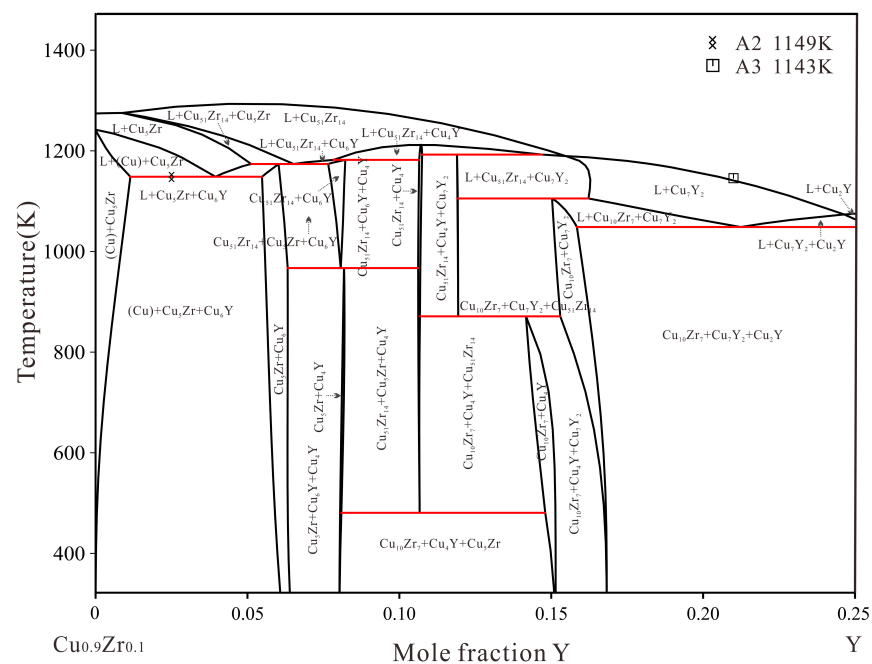

Figure 11. Calculated vertical section of the Cu–Zr–Y system at 10 at.% Zr with the experimental data.

Figure 12. Calculated liquidus projection of the Cu–Zr–Y system with experimental data.

Figure 13. The Scheil simulation for alloys A1 $Cu_{90}Zr_8Y_2$ (at.%) (**a**) and A9 $Cu_{53}Zr_{12}Y_{35}$ (at.%) (**b**).

Based on the CALPHAD method and key experiments, a reasonable set of thermodynamic parameters for the Cu–Zr–Y system was obtained. The thermodynamic parameters were used to simulate phase equilibrium and Scheil solidification, which can guide the design of composition and microstructure of HSHC copper alloy.

5. Conclusions and Summary

The solidification microstructure, phase equilibria and phase transition temperatures in the Cu–Zr–Y ternary system were investigated by XRD, EPMA and DSC technologies. Furthermore, the thermodynamic optimization and a sequence of calculations and simulations using the present thermodynamic parameters were carried out. The major conclusions are as follows:

- The solid solubility in the ternary system is determined. The maximum solubility of Zr in Cu_6Y, Cu_4Y and Cu_7Y_2 are about 6.61, 6.27 and 7.83 at.% Zr, respectively. The solubility of Y in Cu_5Zr, $Cu_{51}Zr_{14}$ and $CuZr$ are about 2.57, 4.45 and 3.38 at.% Y, respectively. The solubility of Cu in the hcp phase is about 2 at.%.
- The Cu–Y system and the Cu–Zr–Y system were optimized by the CALPHAD method. The calculated isothermal sections, liquidus projection and vertical section are consistent with the experimental data.
- The observed solidified microstructure agrees with the result of the Scheil solidification simulations using the thermodynamic parameters. The presently obtained thermodynamic description for the Cu–Zr–Y system can be used to guide the composition and microstructure design of Cu–Zr–Y alloys.

Supplementary Materials: The following supporting information can be downloaded at: https://www.mdpi.com/article/10.3390/ma16052063/s1, Table S1. Summary of the crystallographic data for stable phases in the Cu–Zr–Y system. References [20,27–35] are cited in the supplementary materials.

References

1. Minneci, R.P.; Lass, E.A.; Bunn, J.R.; Choo, H.; Rawn, C.J. Copper-based alloys for structural high-heat-flux applications: A review of development, properties, and performance of Cu-rich Cu-Cr-Nb alloys. *Int. Mater. Rev.* **2021**, *66*, 394–425. [CrossRef]
2. Lin, C.H. Newly-developed Cu(NbZrNx) copper-alloy films for microelectronic manufacture advancement. *Mater. Trans.* **2022**, *63*, 1080–1086. [CrossRef]
3. Qin, Y.Q.; Tian, Y.; Peng, Y.Q.; Luo, L.M.; Zan, X.; Xu, Q.; Wu, Y.C. Research status and development trend of preparation technology of ceramic particle dispersion strengthened copper-matrix composites. *J. Alloys Compd.* **2020**, *848*, 156475. [CrossRef]
4. Zhang, H.T.; Fu, H.D.; Zhu, S.C.; Yong, W.; Xie, J.X. Machine learning assisted composition effective design for precipitation strengthened copper alloys. *Acta Mater.* **2021**, *215*, 117118. [CrossRef]
5. Wang, C.S.; Fu, H.D.; Jiang, L.; Xue, D.Z.; Xie, J.X. A property-oriented design strategy for high performance copper alloys via machine learning. *NPJ Comput. Mater.* **2019**, *5*, 87. [CrossRef]
6. Yang, H.Y.; Ma, Z.C.; Lei, C.H.; Meng, L.; Fang, Y.T.; Liu, J.B.; Wang, H.T. High strength and high conductivity Cu alloys: A review. *Sci. China Technol. Sci.* **2020**, *63*, 2505–2517. [CrossRef]
7. Zhang, P.C.; Shi, J.F.; Yu, Y.S.; Sun, J.C.; Li, T.J. Effect of cryorolling on microstructure and property of high strength and high conductivity Cu-0.5wt.%Cr alloy. *T Nonferr. Metal. Soc.* **2020**, *30*, 2472–2479. [CrossRef]
8. Chen, J.S.; Xiao, X.P.; Guo, C.J.; Yuan, D.W.; Huang, H.; Yang, B. Regulation of primary phase in Cu-Cr-Zr alloy and its effect on nano-structure and properties. *J. Alloys Compd.* **2022**, *926*, 166836. [CrossRef]
9. Peng, L.J.; Xie, H.F.; Huang, G.J.; Li, Y.F.; Yin, X.Q.; Feng, X.; Mi, X.J.; Yang, Z. The phase transformation and its effects on properties of a Cu−0.12wt% Zr alloy. *Mat. Sci. Eng. A-Struct.* **2015**, *633*, 28–34. [CrossRef]
10. Du, Y.B.; Zhou, Y.J.; Song, K.X.; Huang, T.; Hui, D.; Liu, H.T.; Cheng, C.; Yang, J.Z.; Niu, L.Y.; Guo, H.W. Zr-containing precipitate evolution and its effect on the mechanical properties of Cu-Cr-Zr alloys. *J. Mater. Res. Technol.* **2021**, *14*, 1451–1458. [CrossRef]

11. Liu, B.; Zhang, X.B.; Huang, Z.C.; Guo, J.L.; Gong, S.; Xie, G.L.; Peng, L.J.; Li, Z. Microstructure and properties of a novel ultra-high strength, high elasticity and high plasticity Cu-20Ni-20Mn-0.3Nb-0.3Cr-0.1Zr alloy. *J. Alloys Compd.* **2021**, *853*, 157402. [CrossRef]

12. Gao, L.Q.; Yang, X.; Zhang, X.F.; Zhang, Y.; Sun, H.L.; Li, N. Aging behavior and phase transformation of the Cu-0.2 wt%Zr-0.15 wt%Y alloy. *Vacuum* **2019**, *159*, 367–373. [CrossRef]

13. Li, H.H.; Liu, X.; Li, Y.; Zhang, S.H.; Chen, Y.; Wang, S.W.; Liu, J.S.; Wu, J.H. Effects of rare earth Ce addition on microstructure and mechanical properties of impure copper containing Pb. *Trans. Nonferrous Met. Soc. China* **2020**, *30*, 1574–1581. [CrossRef]

14. Li, H.H.; Sun, X.Q.; Zhang, S.Z.; Zhao, Q.Y.; Wang, G.Z. Application of rare-earth element Y in refining impure copper. *Int. J. Min. Met. Mater.* **2015**, *22*, 453–459. [CrossRef]

15. Wang, Y.; Qu, J.; Wang, X.; Jie, J.; Li, T. Effects of Y addition on the microstructure, properties and softening resistance of Cu-Cr alloy. *J. Alloys Compd.* **2022**, *902*, 163816. [CrossRef]

16. Zhang, Y.; Sun, H.L.; Volinsky, A.A.; Wang, B.J.; Tian, B.H.; Chai, Z.; Liu, Y.; Song, K.X. Small Y addition effects on hot deformation behavior of copper-matrix alloys. *Adv. Eng. Mater.* **2017**, *19*, 1700197. [CrossRef]

17. Liu, X.J.; Oikawa, K.; Ohnuma, I.; Kainuma, R.; Ishida, K. The use of phase diagrams and thermodynamic databases for electronic materials. *JOM-US* **2003**, *55*, 53–59. [CrossRef]

18. He, X.C.; Liu, H.S. Determination of the isothermal section of the Cu–Zr–Y ternary system at 978K. *J. Alloys Compd.* **2009**, *475*, 245–251. [CrossRef]

19. Myronenko, P.; Myakush, O.; Babizhetskyy, V.; Kotur, B. Phase equilibria in Y-Zr-Cu system at 870 K. *Visnyk Lviv. Univ. Ser. Chem.* **2011**, *52*, 22–26.

20. Fries, S.G.; Lukas, H.L.; Konetzki, R.; Schmid-Fetzer, R. Experimental investigation and thermodynamic optimization of the Y-Cu binary system. *J. Phase Equilib.* **1994**, *15*, 606–614. [CrossRef]

21. Liu, Y.; Liu, S.; Zhang, C.; Du, Y.; Wang, J.; Li, Y. Experimental investigation and thermodynamic description of the Cu-Zr system. *J. Phase Equilib. Diffus.* **2017**, *38*, 121–134. [CrossRef]

22. Bu, M.J.; Wang, P.S.; Xu, H.H.; Liu, S.H.; Sha, C.S.; Du, Y.; Pan, F.S.; Tang, A.T. Experimental investigation and thermodynamic modeling of the Zr-Y system. *J. Min. Metall. B* **2010**, *46*, 181–192. [CrossRef]

23. Zeng, G.; Hu, B.; Jin, C.G.; Chen, X.J.; Liu, S.H.; Du, Y.; Hu, J.Q. Experimental investigation and thermodynamic assessment of the Ag-Cr-Y and Ag-Cu-Y ternary systems. *Calphad* **2022**, *78*, 102455. [CrossRef]

24. Shi, C.Y.; Liu, Y.L.; Yang, B.B.; Jin, B.; Hu, B.; Rajkumar, V.B.; Du, Y. Phase equilibria thermodynamics and solidified microstructure in the Ag-Cr-Zr system. *J. Alloys Compd.* **2021**, *863*, 158618. [CrossRef]

25. Liu, Y.L.; Zhou, P.; Liu, S.H.; Du, Y. Experimental investigation and thermodynamic description of the Cu-Cr-Zr system. *Calphad* **2017**, *59*, 1–11. [CrossRef]

26. Zhang, Y.; Hu, B.; Li, B.; Zhang, M.; Wang, Q.; Du, Y. Experimental investigation and CALPHAD modeling of the Cu–Cr–Si ternary system. *Calphad* **2021**, *74*, 102324. [CrossRef]

27. Okamoto, H. Cu-Y (Copper-Yttrium). *J. Phase Equilib.* **1992**, *13*, 102–103. [CrossRef]

28. Ellinger, F.H.; Land, C.C. On the plutonium-zirconium phase diagram. *Nucl. Metall.* **1971**, *17*, 686–698.

29. Yasohama, K.; Ogasawara, T. Specific heat and superconducting properties of zirconium-molybdenum alloys. *J. Phys. Soc. Jpn.* **1974**, *36*, 1349–1355. [CrossRef]

30. Forey, P.; Glimois, J.L.; Feron, J.L.; Develey, G.; BECLE, C. Cheminform abstract: Synthesis, characterization and crystal structure of copper-zirconium (Cu$_5$Zr). *Chem. Inf.* **1981**, *12*, 10. [CrossRef]

31. Bsenko, L. Crystallographic data for intermediate phases in the copper-zirconium and copper-hafnium systems. *J. Less-Common Met.* **1975**, *40*, 365–366. [CrossRef]

32. Glimois, J.L.; Forey, P.; Feron, J.; Becle, C. Structural investigations of the pseudo-binary compounds nickel-copper-zirconium (Ni10-xCuxZr7). *J. Less-Common Met.* **1981**, *78*, 45–50. [CrossRef]

33. Carvalho, E.M.; Harris, I.R. Constitutional and structural studies of the intermetallic phase, zirconium-copper (ZrCu). *J. Mater. Sci.* **1980**, *15*, 1224–1230. [CrossRef]

34. Nevitt, M.V.; Downey, J.W. A family of intermediate phases having the Si$_2$Mo type structure. *Trans. Am. Inst. Min. Metall. Pet. Eng.* **1962**, *224*, 195–196.

35. Belyavina, N.N.; Markiv, V.Y.; Nakonechna, O.I. Reinvestigation of the Y–Cu–Ga system at 700°C. *J. Alloys Compd.* **2012**, *541*, 288–296. [CrossRef]

36. Dinsdale, A.T. SGTE data for pure substances. *Calphad* **1991**, *15*, 317–425. [CrossRef]

37. Redlich, O.; Kister, A.T. Algebraic representation of thermodynamic properties and the classification of solutions. *J. Ind. Eng. Chem.* **1948**, *40*, 345–348. [CrossRef]

38. Liu, X.X.; Du, Y.; Liu, S.H.; Pan, Y.F. Measurement of the phase equilibria in the Al-Zr-Y system at 673 and 823 K. *Calphad* **2020**, *68*, 101726. [CrossRef]

39. Bao, X.; Liu, L.; Huang, S.; Jiang, Y.; Wang, X.; Zhang, L. Phase relationships in the al-rich region of the Al-Y-Zr system. *J. Min. Metall. B* **2017**, *53*, 9–12. [CrossRef]

40. Ryan, A.J.; Evans, W.J. The periodic table as a career guide: A journey to rare earths. In *Periodic Table I: Historical Development and Essential Features*; Mingos, D.M.P., Ed.; Springer: Berlin, Germany, 2019; Volume 181, pp. 197–224.

41. Sundman, B.; Jansson, B.; Andersson, J.O. The thermo-calc databank system. *Calphad* **1985**, *9*, 153–190. [CrossRef]

42. Domagala, R.F.; Rausch, J.J.; Levinson, D.W. The systems Y–Fe, Y–Ni, and Y–Cu. *Trans. Am. Soc. Met* **1961**, *53*, 137–155.
43. Qi, G.; Itagaki, K.; Yazawa, A. High temperature heat content measurements of Cu-RE (RE=Y, La, Ce, Pr, Nd) binary systems. *Mater. Trans. JIM* **1989**, *30*, 273–282. [CrossRef]
44. Abend, U.; Schaller, H.J. Constitution and thermodynamics of Cu-Y alloys. *Ber. Bunsenges. Phys. Chem.* **1997**, *101*, 741–748. [CrossRef]
45. Massalski, T.B.; Murray, J.L.; Bennett, L.H. *Binary Alloy Phase Diagrams: Cu-Y.*; Barker, H., Ed.; ASM International, Materials Park: Novelty, OH, USA, 1986; Volume 1.